# 8. FLAT BEAM ADAPTER

The flat beam adapter transformation of an angular momentum dominated was first proposed in the context of electron cooling of high-energy hadron beams [1]. The concept has subsequently been more thoroughly described [2,3] as well as applied to the problem of generation of flat electron beams [4]. In this section, we present a brief overview of the process, and then present an initial design of the optics that achieve the requirements of the proposed facility.

## GENERATION OF THE BEAM IN A SOLENOID FIELD

Electrons are emitted from the photocathode surface into a region of large (~1 kG) solenoidal magnetic field. In the absence of thermal emittance, or finite spread in transverse velocities, the individual electrons would follow paths along the lines of magnetic flux. The influence of a thermal spread in transverse velocities forces the electrons to precess about the magnetic flux lines. The equations of motion for the electrons in this transport channel can be written in so-called 'normal form' that decouples the 4-D transverse phase space into independently evolving 2-D phase spaces. The normal mode variables in this region are drift-cyclotron or 'Larmor' coordinates. This is a 'guiding center' description of the motion of particles in a solenoidal field, which describes the motion of particles not in terms of the absolute Cartesian coordinates $(x, x', y, y')$ or the cylinder coordinates $(r, r', \theta, \theta')$, but rather in terms of the 'drift' position $(d_x, d_y)$ of the Larmor center and 'cyclotron' rotation $(k_x, k_y)$ about the Larmor center (see Figure 8-1). The Larmor coordinates are constructed via the relations

$$\begin{aligned} \vec{k}_\perp &= \left(\vec{\rho}_\perp\right) = \beta_s \begin{pmatrix} x' \\ y' \end{pmatrix}, \\ \vec{d} &= \left(\vec{r} - \vec{\rho}_L\right) = \begin{pmatrix} x \\ y \end{pmatrix} - \frac{\beta_s}{2} \begin{pmatrix} y' \\ -x' \end{pmatrix}. \end{aligned} \tag{1}$$

Here, $\beta_s = eB_z/(2\beta\gamma mc)$ is the equivalent beta-function in the solenoid channel.

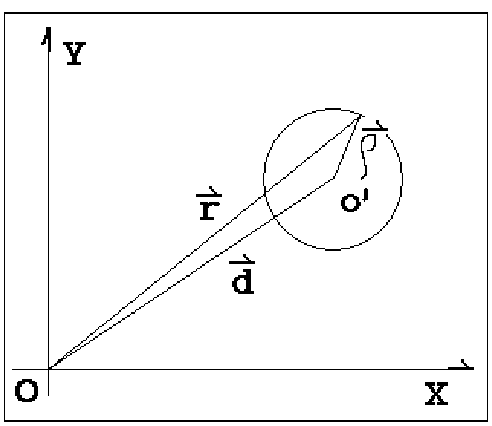


*Figure 8-1    Drift-cyclotron coordinates*

It has been shown that the drift-cyclotron coordinates form canonically conjugate pairs [18], after proper normalization. The 4-D total transverse emittance is constructed from the independent sub-spaces, $\left(d_x, d_y\right)$ and $\left(k_x, k_y\right)$, as

$$\varepsilon_n^2 = \frac{1}{4}\left\langle d^2\right\rangle\left\langle k_\perp^2\right\rangle = \varepsilon_{drift}\varepsilon_{cyclotron}, \tag{2}$$

This is identical to the form described above, but specifically separates the contributions arising from the distinct normal modes. These two contributions can be quantified from parameters arising from conditions at the cathode surface during the emission process. The spot size of the beam at the cathode can be seen to determine the emittance in the drift plane, since $\left\langle d^2\right\rangle$ is proportional to the rms beam spot radius. Finite thermal emittance, originally arising from a distribution of electron velocities with finite spread, is immediately seen to contribute the cyclotron emittance that is proportional to the transverse velocity spread. Depending upon the beam spot radius, the thermal emittance for a $Cs_2Te$ photocathode may vary from ~0.5 to 1.5π mm-mrad. With a solenoid field at the cathode of magnitude ~1 kG, the drift motion emittance may then be much larger than the cyclotron motion emittance. This can also be stated simply that the beam radius is much larger than the characteristic Larmor radius of the individual particle trajectories. This large ratio between drift and cyclotron emittances will be converted to a large ratio between horizontal and vertical emittances following the skew quadrupole adapter.

## EXTRACTION FROM THE SOLENOID FIELD

Exiting the fringe field prepares the beam for the transformation in the skew quadrupole adapter. As the beam passes through the fringe field region at the end of the solenoid lattice, each particle is deflected by the radial magnetic field component. The Cartesian phase-space components are transformed in the thin lens approximation as

$$\begin{pmatrix} x_0 \\ x_0' \\ y_0 \\ y_0' \end{pmatrix}_{\substack{before\\fringe}} \xrightarrow[transformation]{fringe\ field} \begin{pmatrix} x_0 \\ x_0' + y_0/\lambda_s \\ y_0 \\ y_0' - x_0/\lambda_s \end{pmatrix}_{\substack{after\\fringe}} = \begin{pmatrix} x_1 \\ x_1' \\ y_1 \\ y_1' \end{pmatrix}. \tag{3}$$

From the definitions above, the drift and cyclotron coordinates are mapped as

$$\begin{aligned} \vec{k}_{\perp 0} &= \lambda_s \begin{pmatrix} x_0' \\ y_0' \end{pmatrix}_{before} \rightarrow \lambda_s \begin{pmatrix} x_0' + y_0/\lambda_s \\ y_0' - x_0/\lambda_s \end{pmatrix}_{after} = \lambda_s \begin{pmatrix} x_1' \\ y_1' \end{pmatrix} = \vec{k}_{\perp 1}, \\ \vec{d}_0 &= \begin{pmatrix} x_0 - \dfrac{\lambda_s}{2} y_0' \\ y_0 + \dfrac{\lambda_s}{2} x_0' \end{pmatrix}_{before} \rightarrow \begin{pmatrix} \dfrac{3}{2} x_0 - \dfrac{\lambda_s}{2} y_0' \\ \dfrac{3}{2} y_0 + \dfrac{\lambda_s}{2} x_0' \end{pmatrix}_{after} = \begin{pmatrix} x_1 \\ y_1 \end{pmatrix} = \vec{d}_1. \end{aligned} \tag{4}$$

The Cartesian components display coupling between the horizontal and vertical phase spaces after the fringe field transformation. In the laboratory frame, this motion is displayed as a *shear* in the transverse (*x y*) plane.

However, the drift and cyclotron modes are known from the previous section to describe independent degrees of freedom. This still remains the case. The drift and cyclotron degrees of freedom are mapped by the fringe field into independent *circular* modes with oppositely directed angular momenta.

That these are *bona fide* circular modes in the region following the fringe field may be checked by verifying that particle position is transverse to momentum

$$\begin{aligned} \vec{p}_1 &= \left(\beta\gamma mc \cdot x_1', \ \beta\gamma mc \cdot y_1'\right) \\ \vec{r}_1 \cdot \vec{p}_1 &= 0 = \beta\gamma mc\left(x_1 \cdot x_1' + y_1 \cdot y_1'\right) \\ \vec{r}_1 &= \left(x_1, y_1\right) \end{aligned} \tag{5}$$

for each degree of freedom separately. That they are have oppositely-directed angular momenta along the beamline axis ($L_z$) is verified by direct calculation of $L_z = \beta\gamma mc\left(x_1 y_1' - x_1' y_1\right)$ for each independent degree of freedom. For the circular modes derived from the drift and cyclotron motions, the angular momenta are calculated to be

$$\begin{aligned} L_z^{drift} &= -\frac{1}{2} eB_z\left(x_0^2 + y_0^2\right) = -\frac{1}{2} eB_z d_0^2 \ , \\ L_z^{cyclotron} &= \frac{1}{2}\frac{\left(\beta\gamma mc\right)^2}{eB_z}\left(x_0'^2 + y_0'^2\right) = \frac{1}{2}\frac{k_{\perp 0}^2}{eB_z}\left(mc\right)^2. \end{aligned} \tag{6}$$

From this calculation, we see that the drift and cyclotron degrees of freedom are mapped entirely onto independent circular modes with oppositely-directly angular momenta. The product of these two angular momenta is proportional (up to a sign, and factors of *mc*) to the 4-D transverse emittance above. The independent circular mode emittances are merely the magnitudes of their angular momenta (modulo *mc*). Hence, the large ratio between the drift and cyclotron emittances from the previous solenoid channel is recovered in the large ratio between the magnitudes of the angular momenta in the circular modes.

## PASSAGE THROUGH THE SKEW QUADRUPOLE BEAM ADAPTER.

The final step in the process is to pass the beam through the skew quadrupole adapter. We write the coordinates associated with the drift motion as

$$\begin{pmatrix} y_1 \\ y_1' \end{pmatrix}_{drift} = \begin{pmatrix} 0 & \beta_s \\ -1/\beta_s & 0 \end{pmatrix} \begin{pmatrix} x_1 \\ x_1' \end{pmatrix}_{drift} , \tag{7}$$

while the coordinates associated with the cyclotron motion are expressible as

$$\begin{pmatrix} y_1 \\ y_1' \end{pmatrix}_{cyclotron} = \begin{pmatrix} 0 & -\beta_s \\ 1/\beta_s & 0 \end{pmatrix} \begin{pmatrix} x_1 \\ x_1' \end{pmatrix}_{cyclotron} . \qquad (8)$$

The quadrupole adapter lattice is constructed so that the relative betatron phase advance between the $x$ and $y$ phase spaces is $\pi/2$, this condition cancels the remnant coupling between the $x$ and $y$ phase spaces. The adapter transforms the two circular modes into the two planes ($x$, $x'$) and ($y$, $y'$) oriented at 45° with respect to the quadrupoles' normal planes. Thus, in order to transform the drift component in the solenoid into purely horizontal motion, the adapter has to be rotated by 45°. The resulting linear transformation is then written as

$$\begin{aligned} M_{\substack{skew\ quad \\ adapter}} &= M_{\substack{rotation \\ about\ z}}\left(45^\circ\right) \circ M_{\substack{quad \\ lattice}} \circ M_{\substack{rotation \\ about\ z}}\left(-45^\circ\right) \\ &= M_{\substack{rotation \\ about\ z}}\left(45^\circ\right) \circ \begin{pmatrix} 1 & 0 & 0 & 0 \\ 0 & 1 & 0 & 0 \\ 0 & 0 & 0 & -\beta_s \\ 0 & 0 & 1/\beta_s & 0 \end{pmatrix} \circ M_{\substack{rotation \\ about\ z}}\left(-45^\circ\right) \\ &= \frac{1}{2} \begin{pmatrix} 1 & \beta_s & 1 & -\beta_s \\ -1/\beta_s & 1 & 1/\beta_s & 1 \\ 1 & -\beta_s & 1 & \beta_s \\ 1/\beta_s & 1 & -1/\beta_s & 1 \end{pmatrix} \end{aligned} \qquad (9)$$

This linear transformation acts upon the independent cyclotron and drift modes, producing purely vertical and horizontal motions

$$\begin{aligned} M_{\substack{skew\ quad \\ adapter}} \circ \vec{x}_{cyclotron} &= M_{\substack{skew\ quad \\ adapter}} \circ \frac{1}{2} \begin{pmatrix} -\beta_s y_0' \\ x_0' \\ -\beta_s x_0' \\ y_0' \end{pmatrix} = \frac{1}{2} \begin{pmatrix} 0 \\ 0 \\ \beta_s \left[ y_0' - x_0' \right] \\ x_0' + y_0' \end{pmatrix} = \begin{pmatrix} x_v \\ x_v' \\ y_v \\ y_v' \end{pmatrix} = \vec{x}_{\substack{vertical \\ motion}} \\ M_{\substack{skew\ quad \\ adapter}} \circ \vec{x}_{drift} &= M_{\substack{skew\ quad \\ adapter}} \circ \begin{pmatrix} x_0 \\ y_0/\beta_s \\ y_0 \\ -x_0/\beta_s \end{pmatrix} = \begin{pmatrix} x_0 + y_0 \\ \left[ y_0 - x_0 \right]/\beta_s \\ 0 \\ 0 \end{pmatrix} = \begin{pmatrix} x_h \\ x_h' \\ y_h \\ y_h' \end{pmatrix} = \vec{x}_{\substack{horizontal \\ motion}} \end{aligned} \qquad (10)$$

Hence, we see that the cyclotron motion is transformed into purely vertical motion, while the drift motion is transformed to purely horizontal motion. The emittances for these two modes are then

$$\varepsilon^2_{x,horizontal} = \langle x_h^2\rangle\langle x_h'^2\rangle - \langle x_h x_h'\rangle^2 = \frac{1}{\kappa_s^2}\left(\langle x_0^2\rangle + \langle y_0^2\rangle\right)^2 \quad ; \quad \varepsilon^2_{y,horizontal} = 0$$
$$\varepsilon^2_{x,vertical} = 0 \quad ; \quad \varepsilon^2_{y,vertical} = \langle y_v^2\rangle\langle y_v'^2\rangle - \langle y_v y_v'\rangle^2 = \frac{\kappa_s^2}{4}\left(\langle x_0'^2\rangle + \langle y_0'^2\rangle\right)^2 \tag{11}$$

## OBTAINING VERTICAL EMITTANCE SMALLER THAN THE INITIAL THERMAL EMITTANCE

The horizontal and vertical emittances are direct descendants of the emittances of the drift and cyclotron motions (or negative and positive circular mode motions). From the expressions for the horizontal and vertical emittances above, we may write

$$\varepsilon_x = \frac{1}{\kappa_s}\left(\langle x_0^2\rangle + \langle y_0^2\rangle\right) = \frac{eB_z}{2\beta\gamma mc}\left(\langle x_0^2\rangle + \langle y_0^2\rangle\right) ,$$
$$\varepsilon_y = \frac{\kappa_s}{2}\left(\langle x_0'^2\rangle + \langle y_0'^2\rangle\right) = \frac{1}{2}\frac{2\beta\gamma mc}{eB_z}\left(\langle x_0'^2\rangle + \langle y_0'^2\rangle\right). \tag{12}$$

The emittance ratio, then, is [2]

$$\frac{\varepsilon_x}{\varepsilon_y} = 2\frac{(eB_z)^2}{(2\beta\gamma mc)^2}\frac{\langle x_0^2 + y_0^2\rangle}{\langle x_0'^2 + y_0'^2\rangle} = \frac{1}{2}\left(\frac{1}{2}\frac{eB_z}{mc}\right)^2\frac{\langle r_0^2\rangle^2}{\varepsilon^2_{thermal}} = \frac{1}{2}\frac{\langle p_\theta/mc\rangle^2}{\varepsilon^2_{thermal}} , \tag{13}$$

where the thermal emittance is

$$\varepsilon^2_{thermal} = \frac{1}{4}(\beta\gamma)^2\langle x_0^2 + y_0^2\rangle\langle x_0'^2 + y_0'^2\rangle. \tag{14}$$

We can identify a condition by which we can obtain a vertical emittance lower than the initial thermal emittance,

$$\left\langle \frac{p_\theta}{mc}\right\rangle = \frac{1}{2}\frac{eB_z}{mc}\langle r_0^2\rangle > \sqrt{2}\ \varepsilon_{thermal}. \tag{15}$$

Since the thermal emittance is proportional to $\sqrt{\langle r_0^2\rangle}$, the inequality can be satisfied easily by increasing the spot size at the cathode or the magnetic field at the cathode, or both.

This calculation of the horizontal and vertical emittances at the exit of the flat beam adapter assumes that there is no uncorrelated emittance growth along the beamline. The majority of the emittance growth in the beamline is correlated emittance growth between longitudinal slices of the beam. By employing compensation techniques described previously, the correlated emittance increase may be minimized, and the projected emittance at the adapter entrance can be brought near to the lower limit set by the thermal emittance at the cathode.

The remainder of the emittance growth is primarily attributable to intra-beam scattering from space charge effects. This produces growth in the uncorrelated, thermal spread of transverse momenta of the beam electrons. For large drift mode emittance, small changes to the transverse momenta will have little effect. However, the cyclotron mode emittance is proportional to the transverse thermal energy, and it will increase more quickly. The same is true for the horizontal and vertical emittances, respectively, after the adapter. Growth in the uncorrelated (thermal) emittance will impact the vertical emittance more severely than the horizontal, and will drive down the achievable emittance ratio.

## PREVIOUS STUDIES OF FLAT-BEAM TRANSFORMATION – EXISTENCE PROOF

Experiments have been conducted at FNPL [5-7] to demonstrate the technique of flat beam production from a photoinjector. We describe the results of those experiments here.

## Beam Rotation

The beam is observed by CCD cameras viewing aluminum-on-glass OTR screens. A sequence of images at and downstream from the first horizontal slit array with nonzero magnetic field on the cathode, but with zero excitation of the adapter quadrupoles, is shown in Figure 8-2. X3 is located immediately before the entrance to the first skew quadrupole in the adapter lattice, while X4 and X5 are located immediately preceding and following the bunch compressor, respectively. That the beam has angular momentum is demonstrated in the apparent rotation of slit images, and may be measured for comparison with estimates from the theoretical model.

Measurement of the beamlet distributions in the slit images provides a means of determining the vertical emittance (assumed equal to the horizontal since azimuthal symmetry has not been broken), as well as the optical functions of the beam at the location of X3 [8].

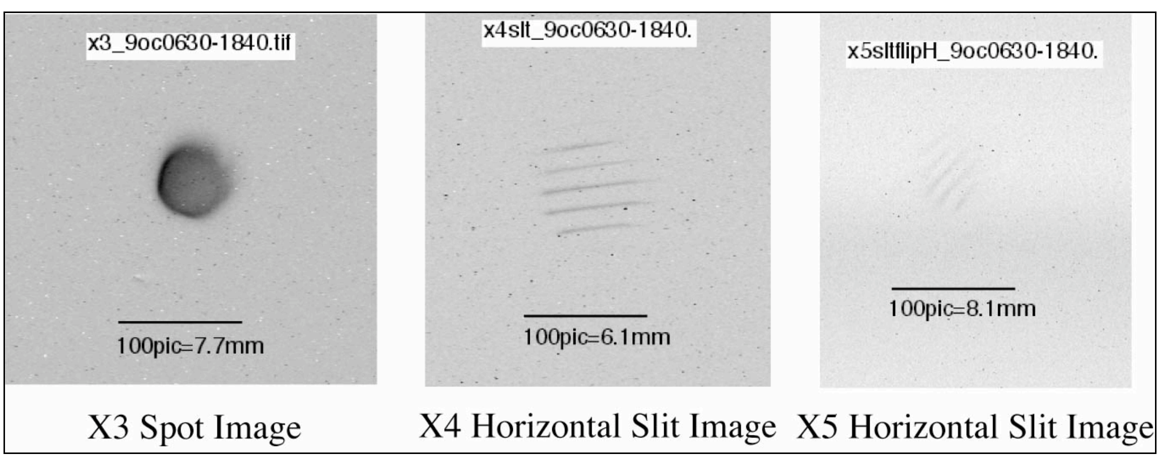


*Figure 8-2 Beam spot at slit analyzer and downstream beamlet images showing angular momentum content of beam.*

## Flat Beam Emittance

Flat beams were produced by energizing the skew quadrupoles shown in Figure 8-1 of section 7-Experimental Studies at FNPL. The beam was observed at various locations along the beamline downstream of the skew quadrupole adapter to ensure that the angular momentum was completely removed. At L6, approximately 3 m downstream from the adapter exit, the beam spot size was measured with an OTR foil. After measuring the spot size, vertical or horizontal analyzer slits were placed into the beamline and the resulting distribution of beamlets was measured at L7 and L8, located approximately 40 cm and 80 cm, respectively, downstream from the analyzer slits. The spot size and beamlet distributions are shown in Figures 8-3 and 8-4.

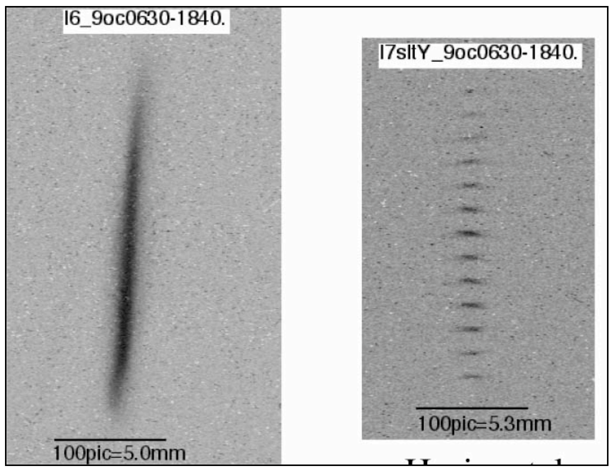


*Figure 8-3 Beam spot image downstream from the adapter (left), and beamlet distribution produced by horizontal slits.*

In these figures, the beam is ‘flat’ in the horizontal plane, with the larger emittance plane in the vertical direction. From slit data in this orientation, the measured ratio of emittances is ~50: 45 $\mu$m (vertical) by 0.9 $\mu$m (horizontal) for a beam with charge ~1 nC. This value is known to be a lower bound on the actual emittance ratio, since the horizontal emittance measurement is resolution limited, as seen in Figure 8-4. The standard deviation of the narrow distribution is comparable to a single pixel of the CCD camera viewing the screen.

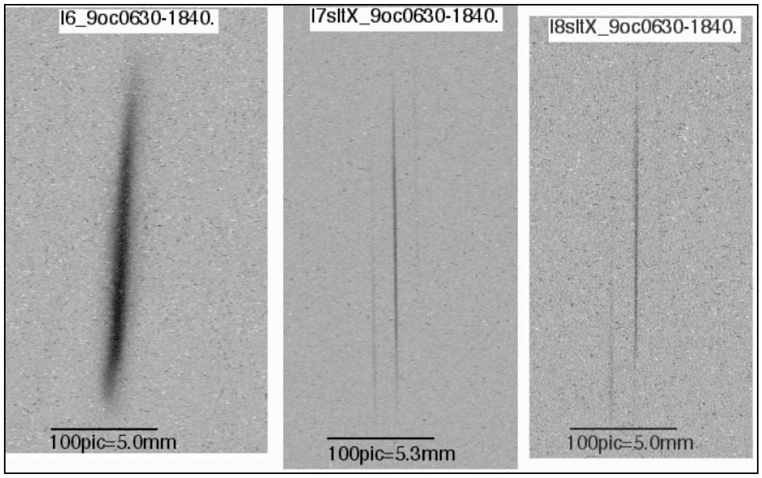


*Figure 8-4 Beam spot image downstream from the adapter (left), and beamlet distribution produced by vertical slits (center and right).*

## Future Work at FNPL

Work at FNPL will continue to explore means of optimizing the flat beam transformation and to explore the available parameter space.

The influence of space charge effects will be decreased with an increase in the laser pulse length from 10 ps to 30 ps. This will primarily affect the space charge induced thermal emittance growth from intra-beam scattering, and thus the growth in cyclotron emittance. However, the effect on the contribution to the projected emittance from correlations between different longitudinal slices must also be studied.

We will carry on parametric studies of emittance compensation and flat beam production. One particular are that will receive more attention in the near future is the sensitivity of the beam emittance to changes in the rf gun gradient and launch phase. We will also study flat beam transforms of higher (>1 nC) charge beams.

The adapter optics and matching will be studied in more detail. The beam optical functions at the adapter entrance will be measured and compared with simulation. We will study via simulation different configurations of the adapter lattice (beyond the three skew quadrupoles) to optimize the flat beam transformation and to minimize the horizontal beam emittance downstream of the adapter.

We will continue working with FNPL personnel to develop diagnostic means of measuring large emittance-ratio beams. The current optical diagnostics are resolution limited, and an increase by a factor of 2-5 is foreseen to measure beams with emittance ratios greater than 50. We will incorporate the measurement diagnostics into our simulations to more accurately model the experiments.

## FLAT BEAM ADAPTER DESIGN

Preliminary studies with PARMELA of the integrated 4-cell rf gun with flat beam adapter have been performed to investigate the sensitivities of lattice geometry and space charge effects to emittance of the resulting beam. These on-going studies are being conducted in parallel with HOMDYN studies of emittance compensation described earlier, and will eventually be combined into an integrated description of the complete beam dynamics in the injector.

In the example shown here, we have simulated the beam dynamics in the rf gun for a particular set of parameters, shown in Table 8-1. The rf fields in this case were calculated with SUPERFISH. For the beam dynamics simulations in the region between the cathode and the entrance to the flat beam adapter, where the beamline still maintains azimuthal symmetry, the 2D (r-z) space charge algorithm was employed.

**Table 8-1: RF Gun parameters for PARMELA simulation**

| | | |
|---|---|---|
| RF gradient (1st cell / 2nd-4th cells) | 64 / 40 | MV/m |
| Beam energy at RF gun exit | 10.22 | MeV |
| Solenoid field (peak / cathode) | 1500 / 1032 | Gauss |
| Bunch charge | 1 | nC |
| Pulse length (FWHM) | 20 | ps |
| Spot size (edge / RMS radius) | 2.4 / 1.7 | mm |
| Thermal emittance (RMS) | 0.7 | π mm-mrad |

The solenoid field profile from the cathode plane ($z$ = 0 cm) to the entrance of the flat beam adapter ($z$ = 100 cm) is shown in Figure 8-5. The beam envelope and radial emittance up to the adapter entrance are shown in Figure 8-6.

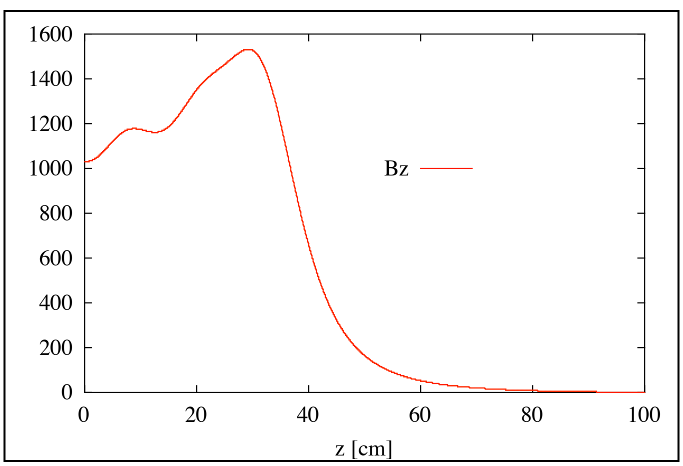


*Figure 8-5 Longitudinal distribution of on-axis solenoid field in rf gun*

With a solenoid field value at the cathode of 1032 Gauss and beam edge radius of 2.4 mm, the canonical angular momentum contributes $(p_\theta/2mc) \sim 44\pi$ mm-mrad to the effective emittance. The theoretical achievable emittance ratio in this configuration is then seen to be $(p_\theta/mc)^2/2\varepsilon_{thermal}^2 \sim 8000$. This simple estimate does not include degradation due to nonlinear space charge and external field influenced emittance growth. Any normal emittance growth experienced between the cathode and the adapter will increase the emittance in the cyclotron degree of freedom and, hence, lower the achievable emittance ratio while raising the lower bound on the achievable vertical emittance.

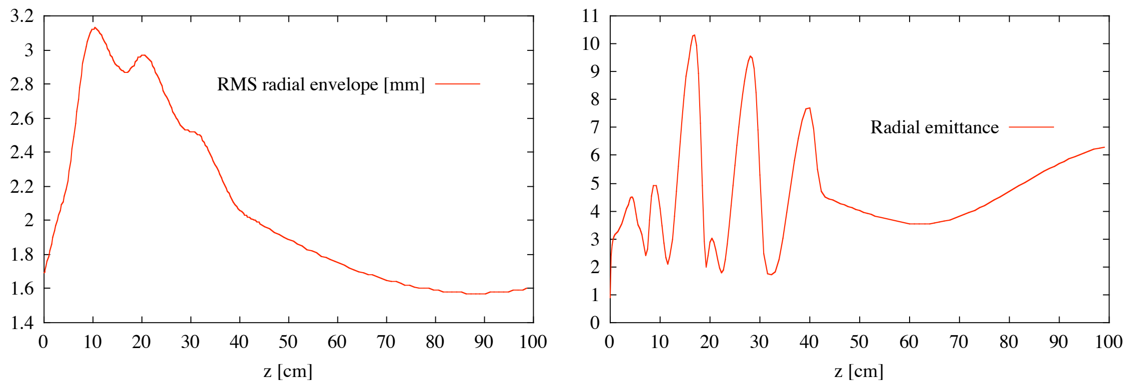


*Figure 8-6 RMS beam envelope (mm) and projected RMS radial emittance (π mm-mrad) (PARMELA)*

At the entrance to the adapter section, PARMELA calculates the drift mode emittance to be ~70π mm-mrad and the cyclotron mode emittance to ~0.097π mm-mrad. The adapter skew quadrupole lattice under consideration here is shown in Figure 8-7.

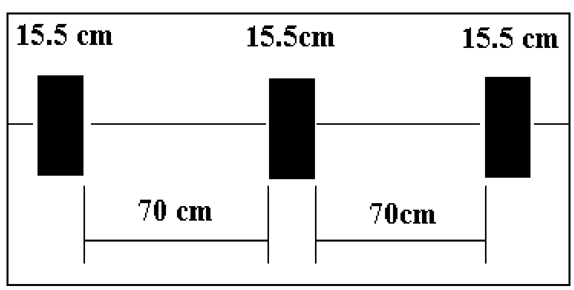


*Figure 8-7 Geometry of skew quadrupole adapter beamline.*

The hard-edged skew quadrupole gradients were determined to be –43.75, 12.5, and –5.88 gauss/cm for the entrance, middle, and exit quadrupoles, respectively. These gradients were determined by minimizing the vertical emittance at the exit of the adapter section, but without the contribution from space charge effects. Once this operating point was found, 3D space charge contributions were added to subsequent PARMELA runs. The horizontal and vertical emittances calculated are listed in Table 8-2.

**Table 8-2  Calculated emittances from PARMELA in the adapter section**

| | $\varepsilon_x$ (π mm-mrad) | $\varepsilon_y$ (π mm-mrad) |
|---|---|---|
| Adapter entrance | 69.754 | 0.097 |
| Exit: No Space Charge | 69.756 | 0.097 |
| Exit: 3D Space Charge | 69.667 | 0.273 |

## Space charge effects

From above example, in the absence of space charge effects in the adapter beamline, the circular mode emittances precisely predict the flat beam emittances. However, with the influence of space charge effects included in the calculation, the vertical emittance almost tripled.

The growth in vertical emittance results from two sources: (i) mismatching of the optical functions in the adapter from linear space charge detuning and  dispersion; and (ii) emittance growth from mismatching the input beam distribution due to nonlinear space charge forces. Our task, then, is to find the optimal working point in the presence of space charge detuning, to calculate emittance growth from nonlinear space charge forces and dispersion, and to devise means of minimizing the emittance growth.

## Non-uniform longitudinal profile – slice effects

The transverse beam distribution at the exit of the adapter beamline can be analyzed with respect to longitudinal position along the bunch. Space charge and dispersion effects in the upstream portion of the injector redistribute the longitudinal profile from uniform to a more parabolic shape. This is shown in Figure 8-8.

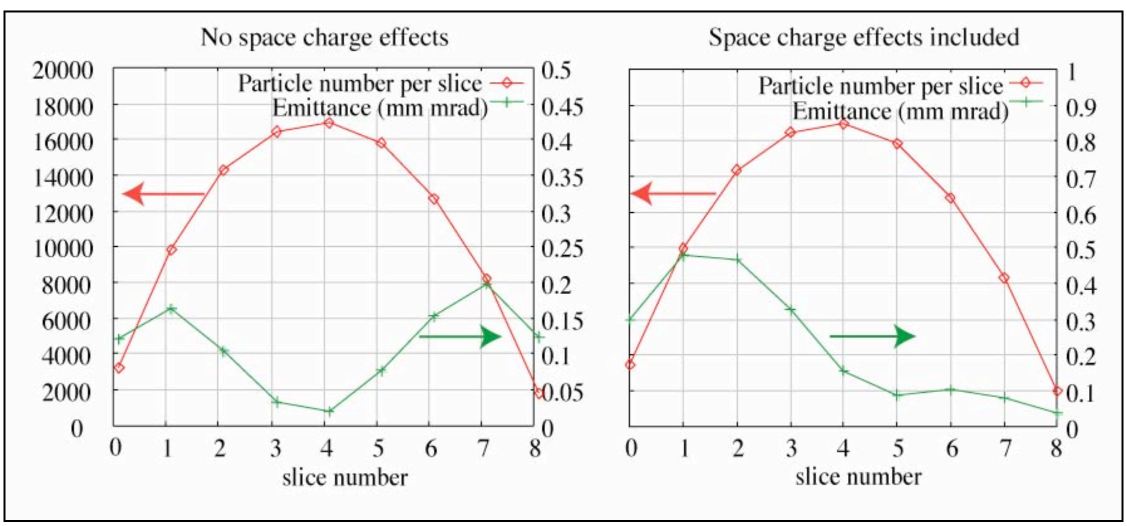


*Figure 8-8    Slice population and transverse emittance at the adapter exit.*

In the absence of space charge effects, the symmetry of the slice emittance distribution at the adapter exit follows that of the longitudinal phase space at the adapter entrance. Figure 8-9 shows the influence of space charge effects in the adapter upon the longitudinal phase space. We see that the correlated energy spread approximately doubles in this region.

## Matching to the adapter lattice

The adapter parameters have been tuned to match the center slice of the beam. From the *y-z* plane view, a dumbbell-shaped distribution is observed. Figure 8-10 shows the head and tail are mismatched with respect to the beam center. They carry residual angular momentum of opposite sign. At the exit of the transformer, the *y-z* beam distribution shows the matching point has shifted towards the tail (and lower energies). The slice emittance in Figure 8-88.8 shows the head contributing more heavily to the projected emittance.

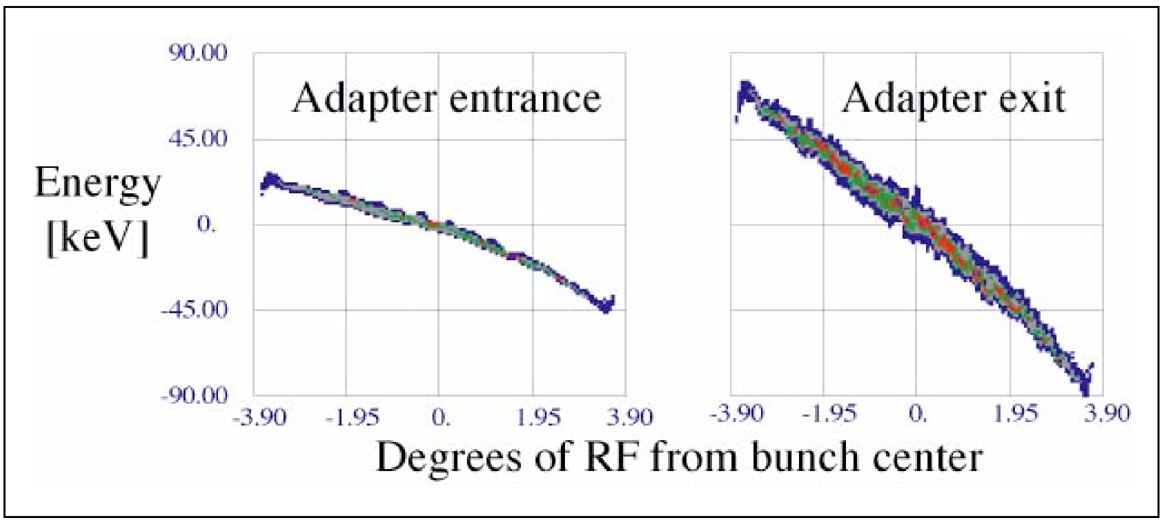


*Figure 8-9 Longitudinal phase space at adapter entrance (z = 100 cm) and exit (z = 286.5 cm).*

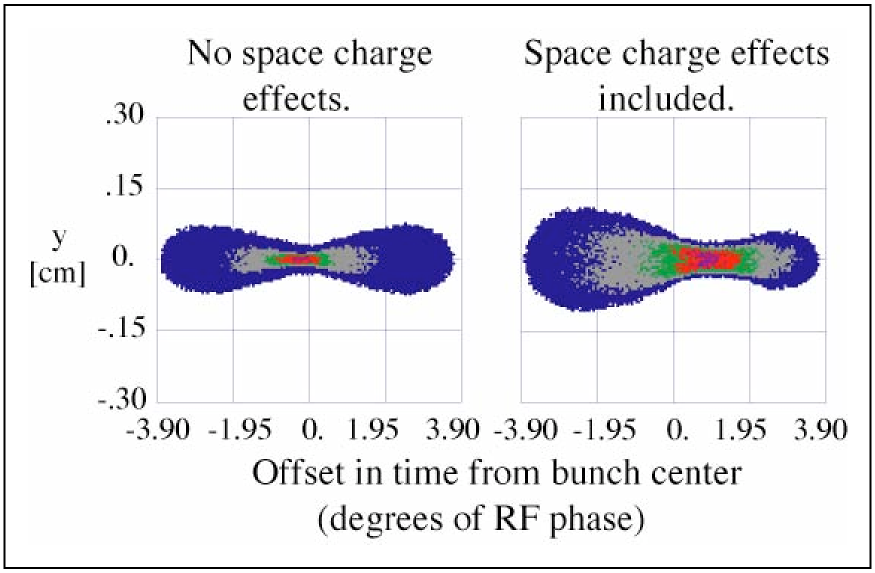


*Figure 8-10 The y-z beam distribution at the adapter exit.*

## Influence of energy mismatch

To study the effect that a mismatch in the beam energy may have on the adapter transformation without the influence of additional space charge effects, we have simulated the beam dynamics through the adapter by intentionally varying energy at which the adapter is matched. In this way, skew quadrupole gradients have been re-optimized for beam energies varying from 10.22 MeV (the nominal value) to 9.50 MeV. The beam (with energy 10.22 MeV) is then re-run through this lattice and the output beam distribution is analyzed (see Figure 8-11).

From these plots, we observe that the matching point shifts from the bunch centroid toward the bunch head as the mismatch energy decreases, with a similar behavior to the effect of space charge detuning.

Adding the influence of space charge effects demonstrates this effect more clearly. In Figure 8. 12, we plot the projected vertical emittance of the beam at the adapter exit, both with and without space charge effects, as a function of the mismatch energy. Without space charge effects, the projected emittance rises monotonically with the degree of mismatch, starting from a matched condition at the nominal energy (10.22 MeV). In the case where space charge effects are included, the optimal condition of the lattice corresponds to an energy of ~9.66 MeV (calculated without detuning effects).

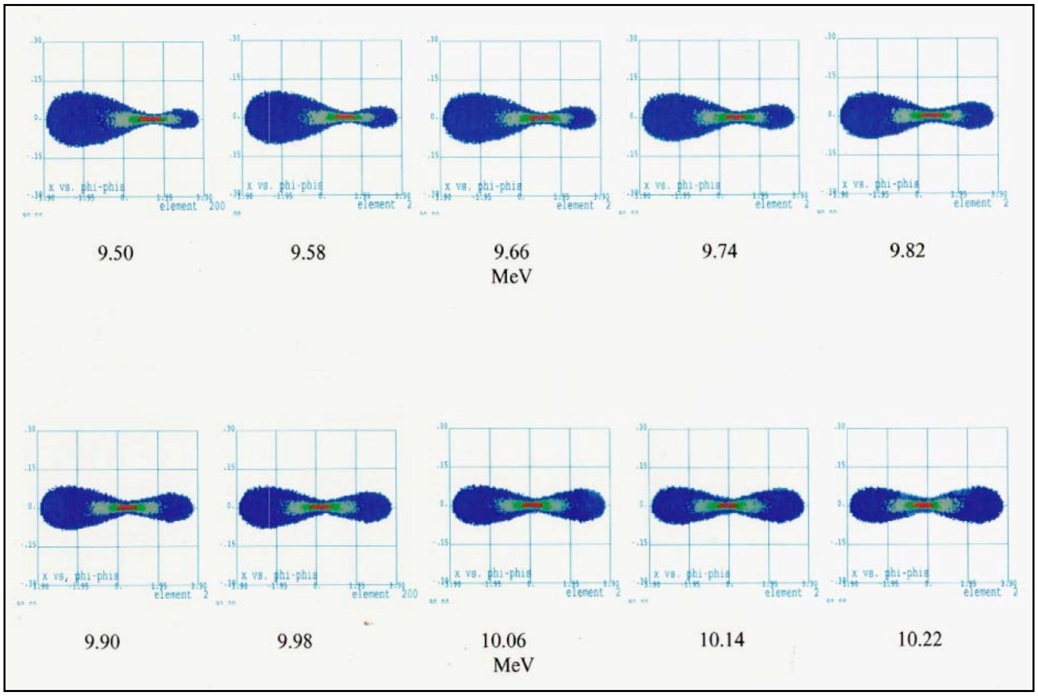


*Figure 8-11 Vertical-longitudinal (y-z) beam distribution under energy mismatch conditions (space charge effects neglected).*

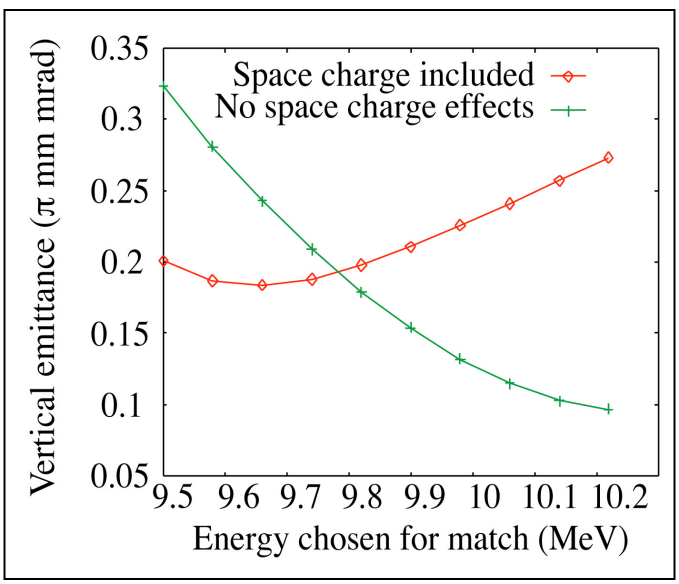


*Figure 8-12 Vertical emittance versus adapter mismatch energy.*

## Discussion of results and future studies

The adapter optics beamline and the beam transport simulations shown here do not yet represent an optimized design. The evolution of the radial emittance in the rf gun and following drift section to the adapter entrance has not been optimized for lowest possible emittance. The adapter entrance is, in fact, located near the secondary local minimum of the radial emittance oscillation. The distribution of slice emittances at the adapter entrance (which matches the distribution at the adapter exit in the absence of space charge effects within the adapter; see Figure 8-8) shows the lack of compensation. However, a slightly different tune of the solenoids around the rf gun will place local emittance minimum at the adapter entrance.

We have demonstrated two effects of space charge on the beam transport in the adapter section. First, the effect of linear space charge tune depression alters the matching condition of the beam within the skew quadrupole adapter lattice such that the beam centroid is matched only for higher quadrupole gradients. The effect of beam charge on the betatron phase advances required for the transformation will be studied. Second, the differences in the correlated sectors of the slice emittances resulting in the variation of cyclotron tunes advance for different slices creates a longitudinally varying mismatch condition along the beam. Again, this may be corrected once emittance compensation is employed to it fullest extent.

The energy spread of the beam at the adapter entrance is roughly ±15 keV, matching the required specifications. However, this value increases by a factor of ~2 by the end of the adapter section. Whether this is due to space charge effects only, or if there is an effect due to the coupled transverse beam distributions transiting the skew quadrupole channel will be studied. For a purely longitudinal space charge effect, this correlated energy spread may be corrected by appropriate phasing of the individual rf gun cavities.

We must assess the impact of different optics and models on the emittance development. The fringe-field at the exit of the solenoid region has not been optimized. Implementing iron field clamps at the exit will cause the fringe to decay more rapidly without affecting the cyclotron tune. The decay of the fringe is responsible, however, for preparing the beam to be injected into the adapter. A more detailed study of the dynamics within the fringe field region needs to be performed and the impact on the emittances clarified. Likewise, the skew quadrupoles used in the adapter will have very significant fringe fields, so that simulation of the beam dynamics within the adapter will need to include the effect of pseudo-multipoles.

## REFERENCES

[1] A.V. Burov and V.V. Danilov, ‘An Insertion to Eliminate Horizontal Temperature of High Energy Electron Beam,’ FERMILAB-TM-2043, 1998.

[2] A. Burov, *et al*., ‘Optical Principles of Beam Transport for Relativistic Cooling,’ FERMILAB-Pub-00/100-T, 2000.

[3] A. Burov, *et al*., ‘Circular Modes, Beam Adapters and their Applications in Beam Optics’, FERMILAB-Pub-01/060-T, 2001.

[4] R. Brinkmann, *et. al*., ‘A Flat Beam Electron Source for Linear Colliders,’ TESLA 99-09, DESY-Hamburg, 1999.

[5] I. Bohnet, *et al.*, 'The Flat Beam Experiment at the FNAL Photoinjector,' *Proceedings of the XX International Linac Conference*, Monterey, 2000.

[6] D. Edwards, *et al.*, 'Status of Flat Electron Beam Production', *Proceeding of the 2001 Particle Accelerator Conference*, (IEEE, New York), 2001.

[7] E. Thrane, *et al.*, 'Photoinjector Production of a Flat Electron Beam,' to appear in *Proceedings of the XXI International Linac Conference*, Gyeongyu, Korea, 2002.

[8] S.G. Anderson, *et al.*, 'Space-charge effects in high brightness electron beam emittance measurements,' Physical Review Special Topics – Accelerators and Beams, **5**, 014201 (2002).